



Identifying AGNs in Low-mass Galaxies via Long-term Optical Variability

Vivienne F. Baldassare^{1,3}, Marla Geha¹, and Jenny Greene²¹ Yale University, Department of Astronomy, 52 Hillhouse Avenue, New Haven, CT 06511, USA; vivienne.baldassare@yale.edu² Princeton University, Department of Astrophysical Sciences, 4 Ivy Lane, Princeton University, Princeton, NJ 08544, USA

Received 2018 August 28; revised 2018 September 28; accepted 2018 October 4; published 2018 December 4

Abstract

We present an analysis of the nuclear variability of $\sim 28,000$ nearby ($z < 0.15$) galaxies with Sloan Digital Sky Survey (SDSS) spectroscopy in Stripe 82. We construct light curves using difference imaging of SDSS g -band images, which allows us to detect subtle variations in the central light output. We select variable active galactic nuclei (AGNs) by assessing whether detected variability is well-described by a damped random walk model. We find 135 galaxies with AGN-like nuclear variability. While most of the variability-selected AGNs have narrow emission lines consistent with the presence of an AGN, a small fraction have narrow emission lines dominated by star formation. The star-forming systems with nuclear AGN-like variability tend to be low mass ($M_* < 10^{10} M_\odot$), and may be AGNs missed by other selection techniques due to star formation dilution or low metallicities. We explore the AGN fraction as a function of stellar mass, and find that the fraction of variable AGN increases with stellar mass, even after taking into account the fact that lower-mass systems are fainter. There are several possible explanations for an observed decline in the fraction of variable AGN with decreasing stellar mass, including a drop in the supermassive black hole occupation fraction, a decrease in the ratio of black hole mass to galaxy stellar mass, or a change in the variability properties of lower-mass AGNs. We demonstrate that optical photometric variability is a promising avenue for detecting AGNs in low-mass, star formation-dominated galaxies, which has implications for the upcoming Large Synoptic Survey Telescope.

Key words: galaxies: active – galaxies: photometry – quasars: supermassive black holes

Supporting material: figure set

1. Introduction

Supermassive black holes (BHs; $M_{\text{BH}} \gtrsim 10^5 M_\odot$) are ubiquitous in the centers of galaxies with stellar masses $\gtrsim 10^{10} M_\odot$. Less is known about the population of BHs in the centers of low-mass galaxies (here defined as galaxies with $M_* \lesssim 10^{10} M_\odot$). However, the population of BHs in low-mass galaxies has the potential to place constraints on the mechanisms by which the seeds of present-day BHs formed. The occupation fraction (i.e., the fraction of galaxies containing BHs) is expected to differ depending on the seed formation mechanisms at play (see the reviews by Greene 2012; Natarajan 2014). In particular, the occupation fraction is sensitive to the seed formation mechanism for galaxies with stellar masses $M_* < 10^{10} M_\odot$.

Detecting BHs in low-mass galaxies poses unique observational challenges. A BH with $M_{\text{BH}} = 10^5 M_\odot$ has a gravitational sphere of influence of just a few parsecs, i.e., largely unresolvable outside the Local Group even with the *Hubble Space Telescope*. In recent years, an increasing number of actively accreting massive BHs have been discovered in low-mass galaxies, particularly using X-ray emission and optical spectroscopic signatures (Greene & Ho 2004, 2007; Barth et al. 2008; Reines et al. 2011, 2013, 2014; Moran et al. 2014; Lemons et al. 2015; Secrest et al. 2015; Mezcuca et al. 2016, 2018; Pardo et al. 2016). However, emission-line ratio diagrams commonly used to identify AGNs were developed using samples of massive galaxies and do not necessarily apply for lower-mass, lower-metallicity systems (Groves et al. 2006; Bradford et al. 2018). Moreover, at low galaxy stellar masses, star formation can dilute the AGN emission-line signal,

resulting in AGNs potentially being missed (Trump et al. 2015). While a sufficiently bright, hard X-ray point source can be a relatively unambiguous signature of an AGN, X-ray imaging down to the relevant luminosities is observationally expensive for large samples (LaMassa 2017). Moreover, below $\sim 10^{40} \text{ erg s}^{-1}$, X-ray emission from an AGN becomes increasingly difficult to distinguish from emission from X-ray binaries, particularly in star-forming galaxies (Lehmer et al. 2010; Mineo et al. 2012; Baldassare et al. 2017b).

Motivated by the potential for identifying systems missed by other selection techniques, we take the approach of searching for AGNs via low-level optical variability. AGNs are known to vary at all wavelengths, and searching for optical variability has been a prolific tool for identifying quasars (e.g., Geha et al. 2003; Sesar et al. 2007; Schmidt et al. 2010; MacLeod et al. 2011; Palanque-Delabrouille et al. 2011; Barth et al. 2014; Choi et al. 2014; Morokuma et al. 2016). The origin of the variability remains uncertain, but is potentially related to thermal instabilities in the accretion disk (e.g., Rees 1984; Kelly et al. 2009). Since the advent of the Sloan Digital Sky Survey (SDSS), great advances have been made in understanding the characteristics of AGN variability, as well as in the identification of AGNs through the presence of variability. Optical variations at the 0.03 mag level have been observed in at least 90% of quasars in the SDSS Stripe 82 (Sesar et al. 2007). Variable AGNs can also be distinguished from other variable objects (such as variable stars) based on their variability properties (Butler & Bloom 2011).

Over the last few years, an increasing number of time domain surveys have come online; an incomplete list includes the Palomar Transient Factory (Rau et al. 2009), Zwicky Transient Facility (Bellm 2014), Pan-STARRS (Chambers et al. 2016; Flewelling et al. 2016), La Silla-QUEST (Cartier et al. 2015)

³ Einstein Fellow.

and *Gaia* (Gaia Collaboration et al. 2016). Additionally, the Large Synoptic Survey Telescope, which will image the entire visible sky every three nights, is scheduled to begin operation in the near future. Given the wealth of available and upcoming time domain data, it is important to assess the utility of variability for identifying AGNs in low-mass galaxies.

Using *g*-band imaging data from the SDSS Stripe 82, we construct light curves for $\sim 28,000$ galaxies in the NASA–Sloan Atlas (NSA), with stellar masses spanning from 10^7 to $10^{12} M_{\odot}$. Section 2 describes the sample and data. Section 3 describes the difference imaging analysis and selection criteria for AGN candidates. In Section 4, we present the full sample of variability-selected AGNs. In Section 5, we discuss the low-mass systems with AGN variability, and present an analysis of the detection limits and expected number of detections for the low-mass end.

2. Sample

Our sample is comprised of galaxies in the NSA which fall within the area of Stripe 82. Stripe 82 is a $\sim 300 \text{ deg}^2$ field near the celestial equator that has been imaged repeatedly by the 2.5 m SDSS telescope. Observations between the years 2000 and 2004 were taken in optimal (photometric) conditions; observations from 2004 to 2008 were taken in a variety of conditions.

The NSA is a reprocessing of the SDSS photometry using the SDSS five-band imaging combined with *Galaxy Evolution Explorer* (*GALEX*) imaging in the ultraviolet (see Blanton & Roweis 2007; Aihara et al. 2011; Blanton et al. 2011; Yan 2011 for details of the SDSS data re/processing techniques). Additionally, the NSA uses an improved background subtraction technique (Blanton et al. 2011), resulting in significantly improved photometry relative to the SDSS DR8 photometric catalog. We use the `nsa_v1_0_1.fits` catalog,⁴ which was released with the SDSS DR13. The v1 catalog extends the NSA out to $z = 0.15$, and adds elliptical Petrosian aperture photometry, using the Petrosian radius from the *r*-band imaging. Aperture corrections have also been applied to the SDSS and *GALEX* photometry. Relevant quantities given in the NSA include spectroscopic redshifts, Petrosian radius, ellipticity, position angle, and stellar mass.

Using the DR13 context in CasJobs, we download all *g*-band images of fields within Stripe 82 ($-1^{\circ}28 < \text{decl.} < 1^{\circ}28$; $\text{R.A.} < 60^{\circ}$ or $\text{R.A.} > 329^{\circ}$). There are 32,206 galaxies in the NSA within the specified R.A. and decl. constraints. As we are trying to detect subtle variations in the nuclear light curves, we only use photometric observations (i.e., SDSS imaging score > 0.6). For our analysis, we restrict our sample to galaxies with more than 10 data points in their light curves (see Section 3). We are unable to generate light curves for 4414/32,206 galaxies, due to either an insufficient number of observations, or poor image subtractions (due to, e.g., an extremely bright foreground star). For the 28,062 for which we construct light curves, the median sample stellar mass is $M_{*} \approx 7 \times 10^9 M_{\odot}$ (assuming $h = 0.70$) and the median sample redshift is $z = 0.09$. The stellar mass and redshift distribution is shown in Figure 1.

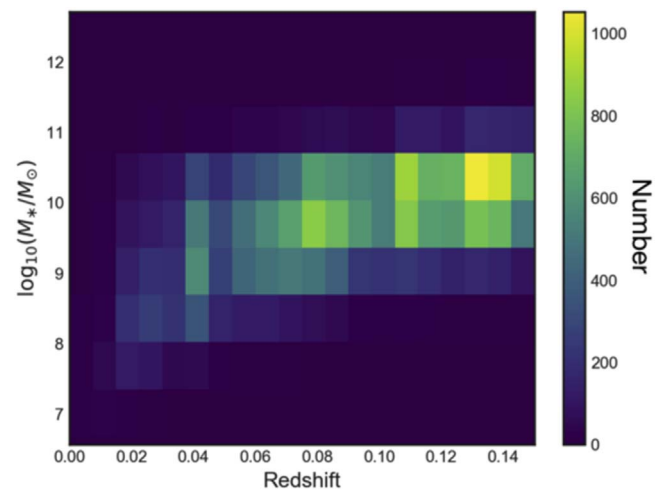


Figure 1. Two-dimensional histogram showing the sample of 28,062 galaxies in both Stripe 82 and the NSA for which we generate light curves, in bins of redshift and stellar mass. Stellar masses are taken from the second release of the NSA catalog.

3. Analysis

3.1. Difference Imaging and Light Curve Construction

Straightforward aperture photometry is insufficient for detecting low-level variations in the light output of a galaxy nucleus. Given that each night of observation has different seeing, simply measuring the flux within a constant aperture means that each observation contains a different fraction of the galaxy starlight in that aperture. The counts measured within a constant aperture depend strongly on the seeing.

Thus, we use difference imaging to construct light curves for each galaxy. Difference imaging, or image subtraction, involves convolving a template image with a kernel to match the seeing and background of an individual observation, and then subtracting one from the other to create a difference image. Specifically, we use the difference imaging software Difference Imaging Analysis Pipeline 2 (DIAPL2),⁵ which is a modified version of the Difference Imaging software introduced by Wozniak (2000). Both are implementations of the basic algorithm introduced by Alard & Lupton (1998) and Alard (2000). The basic steps of our difference imaging procedure are listed below; steps 2 through 4 are carried out within DIAPL2.

1. Crop the SDSS field images to cutouts of 800×800 pixels ($5''3 \times 5''3$) centered around the NSA galaxy. Since fields in different epochs are centered differently, adjacent fields sometimes must be stitched together and then cropped.
2. Align the images, correcting for small pixel shifts between individual frames.
3. Construct a template image consisting of the frames with the best seeing and lowest background. We chose 30% of the frames to be used in the template.
4. For each individual exposure, convolve the template image with a best-fit kernel to match the seeing of the exposure. The kernel is a sum of 2D Gaussians of different widths, and the best-fit parameters are found through chi-squared minimization. The convolved

⁴ <http://www.sdss.org/dr13/manga/manga-target-selection/nsa/>

⁵ <https://users.camk.edu.pl/pych/DIAPL/>

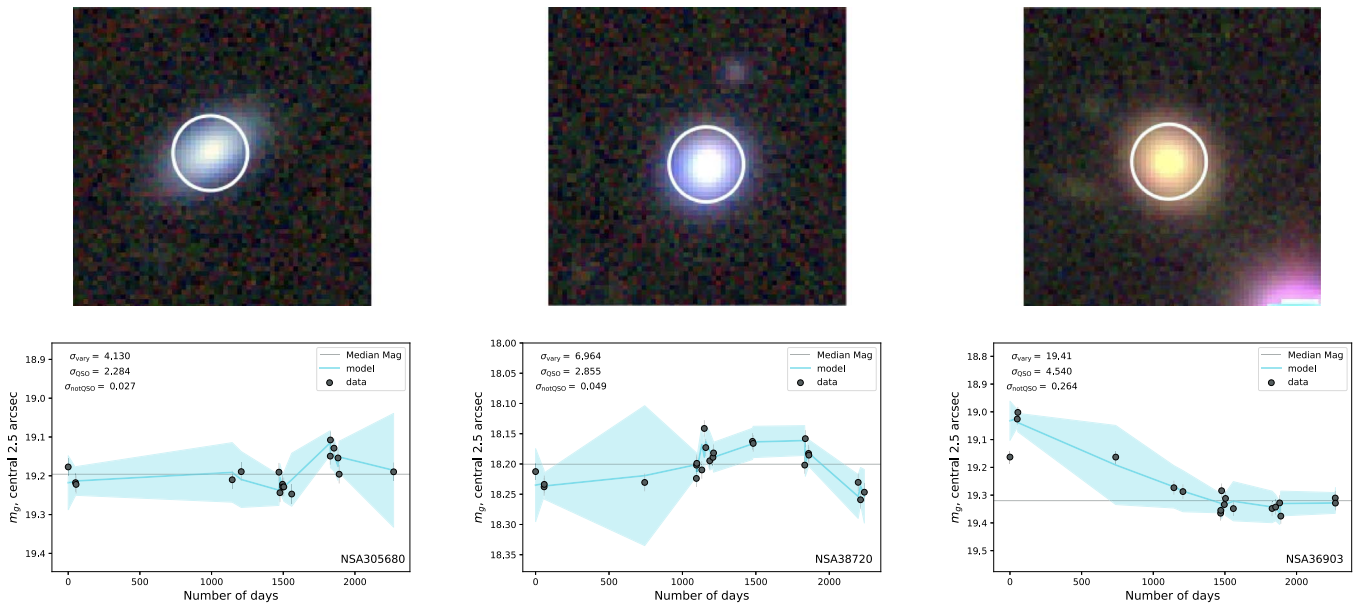


Figure 2. Examples of galaxies which meet our AGN selection criteria ($\sigma_{\text{var}} > 2$ and $\sigma_{\text{QSO}} > 2$). The top panel shows DECaLS images (<http://legacysurvey.org/viewer>) with a circle of radius $2''.5$ over the nucleus as given in the NSA. The images are $20''$ across. The lower panel shows the nuclear g -band light curve. The gray points are the observed nuclear g -band magnitudes with corresponding errors. The blue solid line shows the best-fit damped random walk model from `qso_fit`, and the light blue shaded region shows the model uncertainties.

template is then subtracted from the exposure to create the difference image.

5. Construct a light curve using forced photometry of template and difference images. Since we are searching for variability from a point source, photometry is done on a $2''.5$ circle at the position of the galaxy nucleus as defined in the NSA. The $2''.5$ aperture is chosen to be slightly larger than the worst-case scenario seeing, so as not to miss any light from the galaxy nucleus. The flux value for each epoch is the value measured in the template plus that measured in the difference image.

3.2. Selection of AGN Candidates

AGN light curves are well-modeled by a damped random walk (Kelly et al. 2009; MacLeod et al. 2010, 2011; Butler & Bloom 2011). The damping functions to push deviations back toward a mean value, as opposed to the variance simply continuing to increase over time.

After constructing each light curve, we use the Butler & Bloom (2011) quasar fitting software `qso_fit`⁶ to determine whether the light curves are variable, and whether the observed variability is characteristic of an AGN. Butler & Bloom (2011) define a covariance matrix C which well-describes AGN variability as a function of time. It is then possible to write down the probability of observing some data x given the AGN variability model C . Specifically, the `qso_fit` code creates a model light curve by modeling each point given the other points and the covariance matrix describing the variability. It then assesses how well the best-fit damped random walk model describes the data.

We compute several fit statistics, including χ^2/ν (standard measure of variability), $[\chi^2/\nu]_{\text{QSO}}$ (the fit statistic for the fit of the data to a damped random walk model), and $[\chi^2/\nu]_{\text{null}}$ (the

expected fit statistic for a non-AGN variable source). We also compute σ_{var} (the significance that the source is variable), σ_{QSO} (the significance that $[\chi^2/\nu]_{\text{QSO}} < [\chi^2/\nu]_{\text{null}}$), and σ_{notQSO} (the significance the source variability is not AGN-like).

First, we select objects with a variability significance $\sigma_{\text{var}} > 2$ and a QSO significance $\sigma_{\text{qso}} > 2$ (i.e., the significance that the source is variable and that the fit to the damped random walk model is better than the fit to a randomly variable model are $>2\sigma$). Of the 28,062 total galaxies with light curves, 201 meet these AGNs variability selection criteria.

We then inspect light curves by eye to remove objects that are identified as variable due to poor image subtractions or likely supernovae (SNe) missed by the variance and QSO light curve cuts. Of the 201 galaxies that initially meet our selection criteria, we find that 29 of them are SN-like (i.e., show one frame with a bright nucleus, or an obvious rise and fall on a SN-like timescale), 15 are mischaracterized in some way in the NSA (i.e., are either stars or higher-redshift AGNs), and 21 have problematic image subtractions, such as interference from a nearby saturated star. One system—NSA 29189—has AGN-like variability but is classified in the literature to contain a luminous blue variable star (Izotov & Thuan 2009). This leaves 135 variability-selected AGNs. In Figure 2 we show examples of galaxies with AGN-like variability. Figure 3 shows examples of objects with variable light curves uncharacteristic of an AGN, and Figure 4 shows galaxies initially classified as AGNs that have SN-like light curves.

Figure 5 shows a two-dimensional histogram of light curve standard deviation (σ_{LC}) versus median nucleus magnitude (with the nucleus defined as the central $2''.5$). The light curve standard deviation corresponds to the 1σ scatter about a light curve median value. All of the objects identified as variable AGNs by our criteria also happen to have σ_{LC} more than one standard deviation above the typical σ_{LC} for nuclei of the same magnitude.

⁶ http://butler.lab.asu.edu/qso_selection/index.html

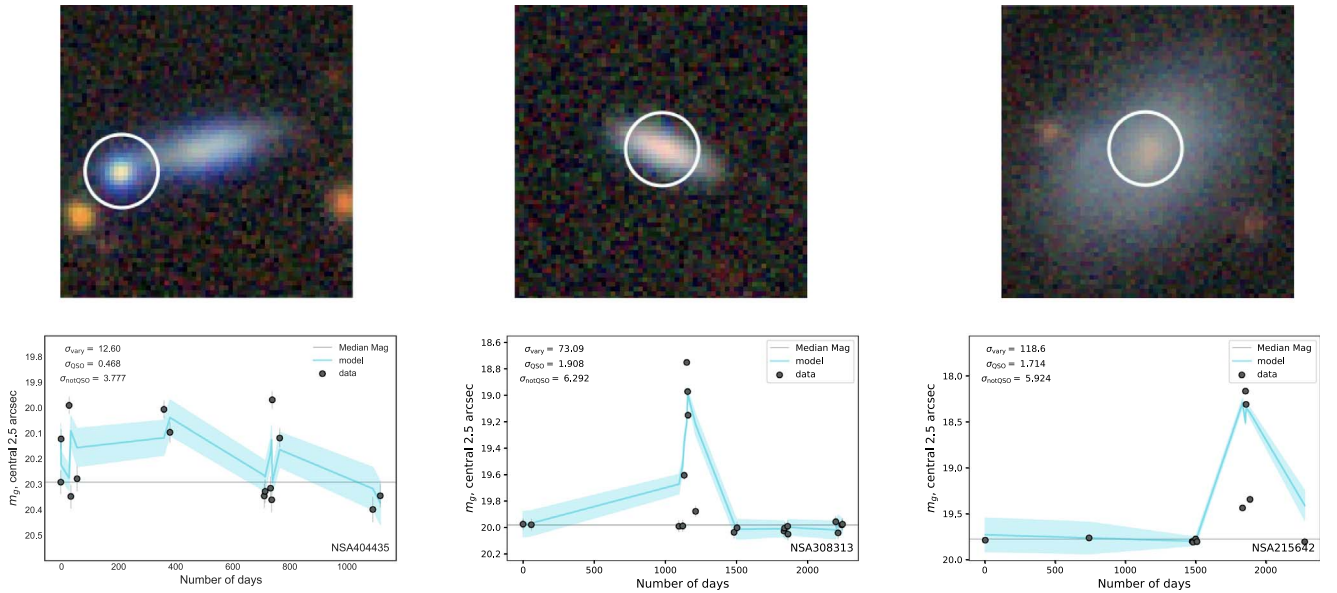


Figure 3. Same as Figure 2, but with examples of galaxies which have variable light curves which are classified as uncharacteristic of an AGN ($\sigma_{\text{var}} > 2$ and $\sigma_{\text{notQSO}} > 2$). The top panel shows DECALs images with a $2''$ circle over the nucleus. The lower panel shows the nuclear g -band light curve.

3.2.1. Other Variable Objects

In addition to the variable AGNs, there are 2650 galaxies that have $\sigma_{\text{var}} > 2$ and $\sigma_{\text{QSO}} < 2$. These objects tend to fall in one of three categories: stars misclassified in the NSA, genuinely variable objects that are not AGNs, and objects with poor image subtractions. When comparing the distribution of the number of data points for the full sample to that for objects with $\sigma_{\text{var}} > 2$ and $\sigma_{\text{QSO}} < 2$, the latter skews toward a lower number of data points. This is likely due to the fact that fewer frames generally result in a worse image subtraction. However, it is possible that some are variable AGNs that are missed due to poor light curve sampling.

We explore the effect of reducing the number of light curve points on our ability to detect variability by taking variable light curves with more than 20 data points, removing a specified number of data points, and then re-running the light curve analysis. We randomly remove data points to create light curves with 10 and 15 data points, and re-run the analysis. This is done 2000 times each for light curves containing 10 and 15 points. The results vary widely depending on the AGN light curve. For example, for NSA 37000 (23 data points; $\sigma_{\text{var}} = 25.4$; $\sigma_{\text{QSO}} = 5.6$), it is classified as a variable AGN 98.5% of the time with 15 data points, and 87% of the time with 10 data points. For NSA 40018 (24 data points; $\sigma_{\text{var}} = 31.5$; $\sigma_{\text{QSO}} = 4.2$), it is classified as a variable AGN 81% of the time with 15 data points, and 65% of the time with 10 data points. However, they are virtually always found to have $\sigma_{\text{var}} > 2$; the AGN significance tends to fall with decreasing numbers of data points. We require a minimum of 10 data points for our light curve analysis; the median number of data points in a given light curve in our sample is 17. None of our conclusions are affected by the loss of variable AGNs due to sampling, though our sample of variability-selected AGNs is certainly not complete.

3.3. Spectroscopic Analysis

We analyze SDSS spectroscopy for our variability-selected AGN. If a galaxy has more than one spectrum, we use the primary

spectrum designated by the SDSS. In particular we measure emission-line fluxes and search for broad $H\alpha$ emission potentially indicative of dense gas orbiting around a central BH. Here, we describe the emission-line modeling procedure (see also similar fitting procedures described in Ho et al. 1997; Greene & Ho 2004; Reines et al. 2013; Baldassare et al. 2015, 2016).

We first create a model for the narrow-line emission using the intrinsically narrow [S II] $\lambda\lambda 6713$ and 6731 lines. As these are forbidden transitions, they are guaranteed not to be produced in the denser broad-line region gas. This narrow-line model is then used to fit the narrow $H\alpha$ emission and the [N II] $\lambda\lambda 6548$ and 6684 lines simultaneously. We allow the width of narrow $H\alpha$ to increase by up to 25% and fix the relative amplitudes of the [N II] lines to laboratory values. Next, an additional Gaussian component representing the broad $H\alpha$ emission is added to the model. If the χ^2 value of the fit improves by 20%, the broad component is kept in the model. We allow up to two Gaussian components to be used to model the broad emission.

We also fit $H\beta$, [O III] $\lambda 5007$, [O III] $\lambda 4959$, and the [O II] $\lambda\lambda 3726, 3729$ doublet. We also allow $H\beta$ to be fit with an additional (broad) Gaussian component. In all of our emission-line fitting, the continuum is modeled simply as a line across the relevant spectral region.

4. Variability-selected AGNs

We find 135 galaxies with AGN-like optical photometric variability (see Section 3.2 for the selection criteria). The variability amplitudes range from ~ 0.01 to 0.25 mag, with a median 1σ variability of 0.05 mag. Apparent g -band magnitudes of the nuclei range from 15 to 20.5 mag. The detectable level of variability depends on the apparent magnitude of the nucleus, as shown in Figure 5. In the following, we discuss the host galaxy properties and spectroscopic properties.

4.1. Host Galaxy Properties

The host galaxies of the variability-selected AGNs range from $\sim 2 \times 10^8$ to $5 \times 10^{11} M_{\odot}$ in stellar mass. Figure 6

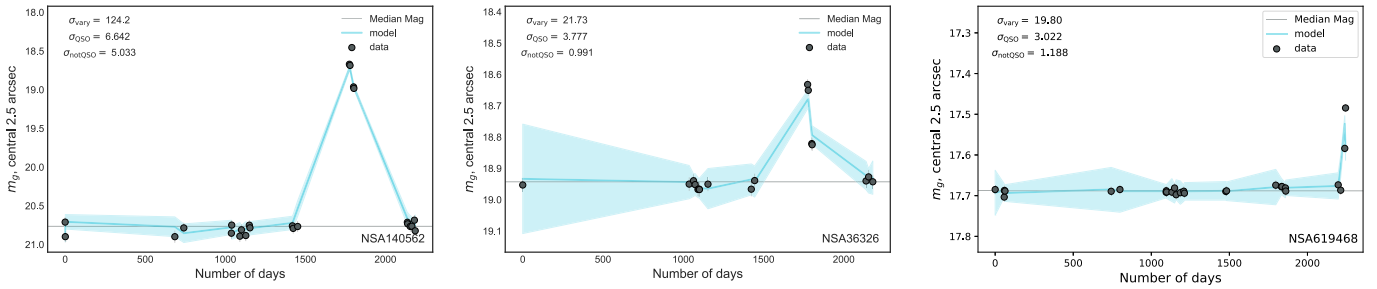


Figure 4. Examples of galaxies with SN-like light curves which were classified as having AGN-like variability by our selection criteria. These light curves are relatively constant but for a few elevated points which rise and/or fall on SN-like timescales.

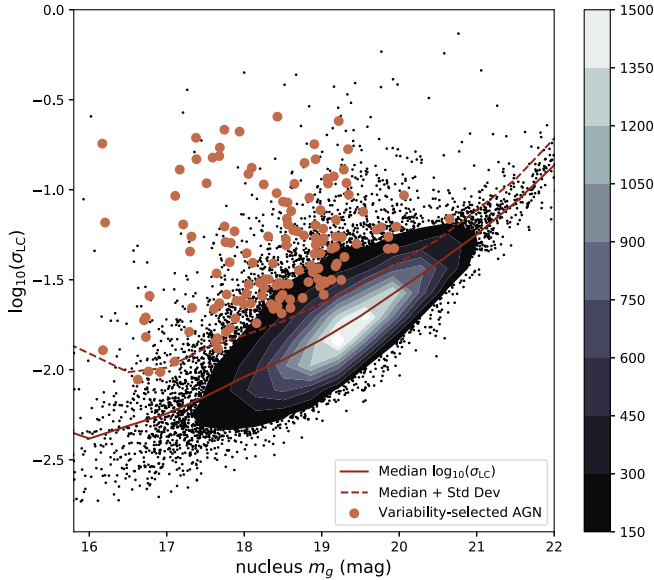


Figure 5. Root-mean-square scatter about the light curve median value (σ_{LC}) vs. the median nucleus g -band magnitude. The contour shading corresponds to the number of objects. The scatter for a given light curve increases for fainter galaxies due to larger flux uncertainties. Galaxies selected as having AGN-like variability are shown as orange circles. The median σ_{LC} value for a given magnitude is shown by the solid red line, and the values of σ_{LC} which are one standard deviation from the median are shown by the dashed red line. Note that the variability-selected AGNs have σ_{LC} values at least $\sim 1\sigma$ above the typical value for their magnitude bin.

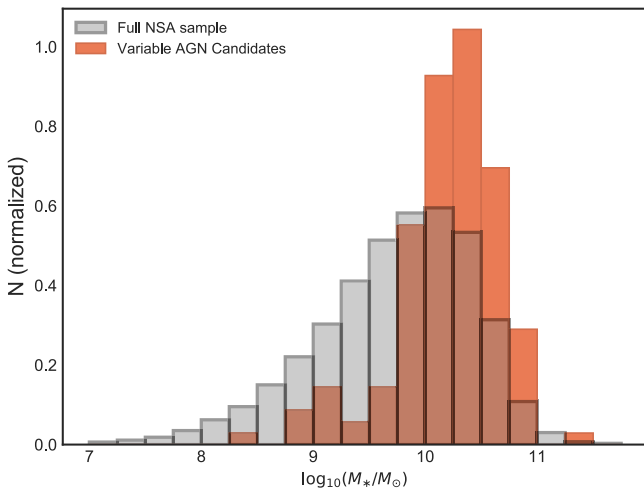


Figure 6. Normalized histogram showing the stellar mass distribution of the full NSA parent sample (gray), and of the variability-selected AGNs (orange). The sample of variability-selected AGNs skews toward a higher stellar mass than the underlying parent sample.

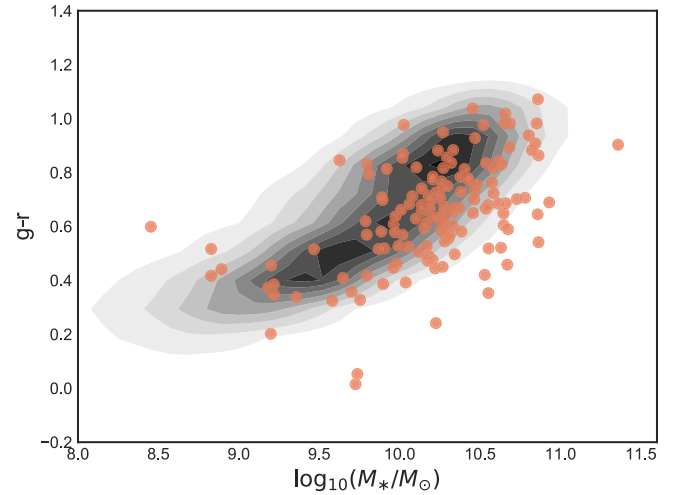


Figure 7. Host galaxy $g - r$ color vs. stellar mass. Colors were computed using the elliptical Petrosian fluxes given in the NSA, and have been corrected for extinction. The gray contours show the entirety of the NSA sample for which we were able to construct light curves. The variability-selected AGNs are shown as orange data points; overall, these tend to be bluer than non-variability-selected galaxies at a given stellar mass.

shows the stellar mass distribution of the 135 variability-selected AGN hosts as compared to the parent sample of $\sim 28,000$ galaxies in the NSA for which we construct light curves. The variability-selected AGNs tend toward higher stellar mass; the median stellar mass of the variability selected AGNs is $1.8 \times 10^{10} M_{\odot}$, while the parent sample has a median stellar mass of $6.8 \times 10^9 M_{\odot}$. We show the host galaxy $g - r$ colors in Figure 7. The $g - r$ colors of the variability-selected AGNs range from 0.01 to 1.1, and as a sample tend to be bluer than the parent population (see also Matsuoka et al. 2014).

The properties of the NSA/Stripe 82 AGNs identified in this work are consistent with those found for a sample of 975 variability-selected AGNs from the Pan-STARRS1 Medium Deep Survey, which consists of 10 7-deg² fields imaged in the same filter every three nights (Heinis et al. 2016) down to a limiting magnitude of ~ 23.5 . To compile their sample of AGNs, they began with a sample of 4361 extragalactic variable sources, which were then further classified as AGNs or SNe (Kumar et al. 2015). While not all objects in their sample have spectroscopic information, they find that the masses of the variability-selected AGN skew high as compared to the general population of galaxies. Their distribution of host galaxy masses peaks near $\log_{10}(M_{*}/M_{\odot}) = 10.6$, similar to our results (Figure 6). They also find that their AGN hosts tend to be bluer than the general population.

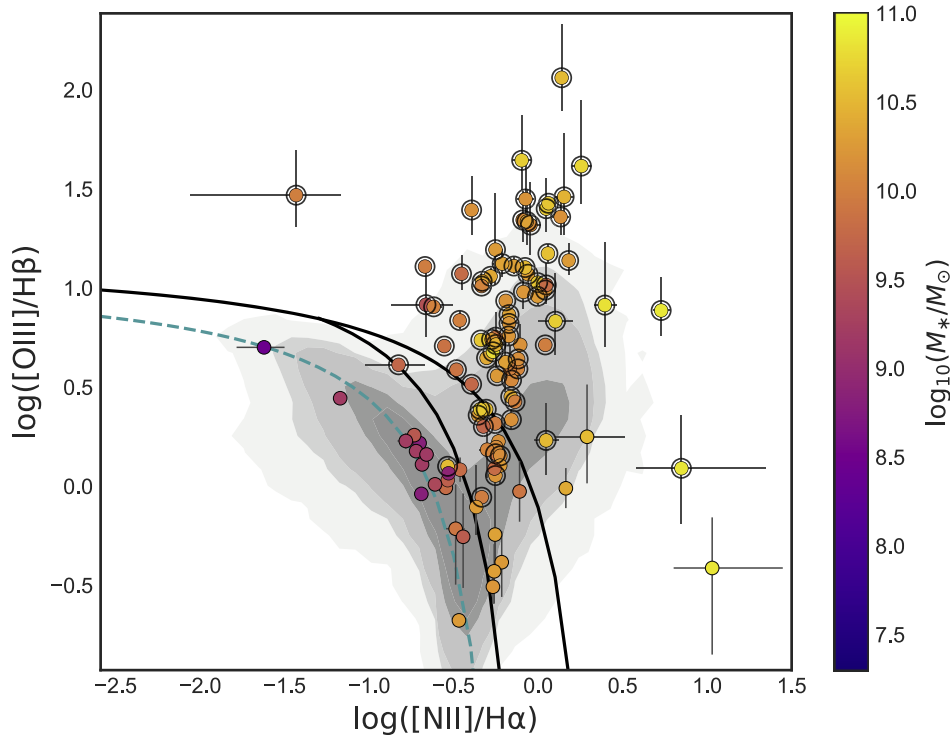


Figure 8. BPT diagram showing the positions of the variability-selected AGNs. The black lines show the traditional BPT diagram separation lines (Baldwin et al. 1981; Kewley et al. 2001, 2006), and the blue dashed line shows the star-forming main sequence (Kewley et al. 2013). Data points are color-coded by galaxy stellar mass, obtained from the NSA. 100 galaxies reside in the AGN or composite regions of the BPT diagram, while 20 are in the star-forming region.

4.2. Spectroscopic Properties

We show where the variability-selected AGNs sit on the Baldwin–Phillips–Terlevich (BPT) diagram (Baldwin et al. 1981) in Figure 8. We plot only galaxies which have signal-to-noise ratio $\gtrsim 2$ for all of $H\beta$, $[O\text{ III}] \lambda 5007$, $H\alpha$, and $[N\text{ II}] \lambda 6584$ (104 galaxies). Of the 104 galaxies, 86 of them (83%) have narrow emission-line ratios placing them in the AGN or composite regions of the BPT diagram (21 BPT composites and 65 BPT AGNs). Interestingly, 18 galaxies (or 17% of the spectroscopic sample) have narrow emission-line ratios dominated by star formation. These galaxies tend to be the lowest-mass systems in our sample. Only two of the 18 in the star-forming region have stellar masses greater than $10^{10} M_{\odot}$; the median stellar mass for these 18 objects is $1.7 \times 10^9 M_{\odot}$.

We also search for broad $H\alpha$ emission indicative of dense gas orbiting around the central BH. We find that 82/135 of the galaxies with AGN-like variability (61%) have broad $H\alpha$ emission lines. Of the objects with narrow lines in the composite/AGN regions, $\sim 80\%$ also show broad $H\alpha$. We estimate single-epoch virial BH masses using the broad $H\alpha$ FWHM and luminosity (Greene & Ho 2005). The FWHM of the broad component gives a characteristic velocity of gas in the broad-line region, and the distance to this region is correlated with the continuum luminosity at 5100 \AA (Bentz et al. 2009, 2010, 2013), which in turn is correlated with the luminosity of broad $H\alpha$. BH masses estimated in this way have systematic uncertainties of roughly 0.3 dex (or a factor of ~ 2). Specifically, we use the BH mass formula given in Reines et al. (2013). The broad $H\alpha$ luminosities range from $\sim 1 \times 10^{39}$ to $3 \times 10^{42} \text{ erg s}^{-1}$ and the FWHMs range from ~ 900 to 6500 km s^{-1} . We calculate BH masses ranging from 1×10^6 to $1 \times 10^8 M_{\odot}$, and the median $M_{\text{BH-to-}M_{*}}$ ratio is 8×10^{-4} ,

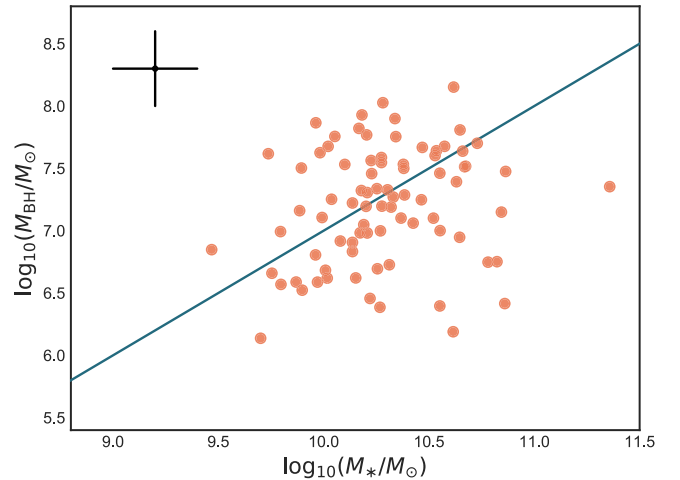


Figure 9. Black hole (BH) mass vs. stellar mass for objects with broad $H\alpha$ emission. The black point in the upper left-hand corner shows the typical BH mass uncertainty (~ 0.3 dex) and stellar mass uncertainty (~ 0.2 dex). The solid blue line corresponds to the canonical BH-to-stellar mass ratio of 0.001 (Kormendy & Ho 2013).

close to the canonical value of 0.001 (Kormendy & Ho 2013). However, there is considerable scatter about this value, as shown Figure 9. Fitting a linear regression to the $M_{\text{BH-to-}M_{*}}$ relation for these objects gives a slope that is consistent with zero.

4.3. Variable AGN Fraction versus Stellar Mass

We present the measured active fraction (i.e., the fraction of galaxies with AGN-like variability) as a function of stellar mass in the left panel of Figure 10. At face value, Figure 10 suggests that there is a steep increase in the fraction of variable AGNs as a

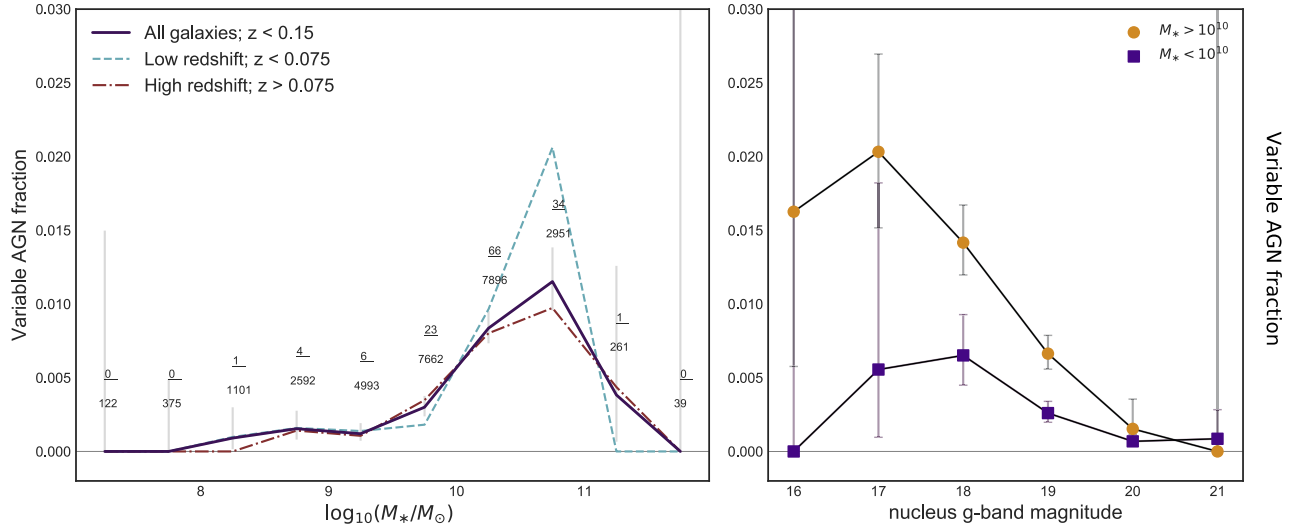


Figure 10. Left: variable AGN fraction vs. stellar mass. The active fraction corresponds to the fraction of galaxies with nuclear variability consistent with the presence of an AGN (see the text for details). The solid purple line shows the full sample with $z > 0.15$, while the dashed blue and dashed-dotted red lines show the sub-samples with $z < 0.075$, and $z > 0.075$, respectively. Also shown are the number of detections over the total number of galaxies in each bin, for the full sample out to $z = 0.15$. Right: active fraction vs. median light curve g -band magnitude for galaxies with $M_* > 10^{10} M_\odot$ (blue circles) and $M_* < 10^{10} M_\odot$ (orange squares). The active fraction is computed in bins one magnitude wide; the plotted magnitude value is the center of each bin. Uncertainties are computed assuming a binomial distribution and correspond to a 1σ confidence limit.

function of stellar mass. However, there are a number of observational biases which must be taken into account. As shown in Figure 5, lower levels of variability are detectable in brighter nuclei. The median nucleus g -band magnitude for the $M_* > 10^{10} M_\odot$ sample is ~ 18.5 , while for galaxies with $M_* < 10^{10} M_\odot$ the median magnitude is ~ 19.5 . The right side of Figure 10 shows the active fraction as a function of nucleus g -band magnitude for two different mass bins. At a given nucleus magnitude, the active fraction tends to be lower for low-mass galaxies than for higher-mass galaxies (see Section 6 for a discussion of potential explanations). At $m_g \approx 18$, the variable AGN fraction is roughly twice as high in the sample with $M_* > 10^{10} M_\odot$ than for the low-mass sample (Table 2).

5. Variability as a Tool for Identifying AGNs in Low-mass Galaxies

Above stellar masses of $10^{10} M_\odot$, virtually all of the variability-selected AGNs are also narrow-line AGNs. However, at $M_* < 10^{10} M_\odot$, roughly half of the sample has narrow emission-line ratios dominated by star formation (see Figure 8). Motivated by the potential for using low-level optical variability to identify low-mass AGNs, in this section we examine further the 35 “low-mass” ($M_* < 10^{10} M_\odot$) galaxies with AGN-like variability and explore how they compare to low-mass AGNs identified via other techniques. We caution that these objects should generally be regarded as candidates; deeper, higher spatial resolution spectroscopic follow-up is underway for this sample to better isolate emission from the nucleus. All variability-selected galaxies with $M_* < 10^{10} M_\odot$ are listed in Table 1. The galaxies range in $g - r$ color from $\sim 0 - 1$, with a median $g - r = 0.46$. See Figure 12 for images and light curves for all objects with $M_* < 10^{10} M_\odot$.

5.1. SDSS Detection Limit

In order to determine what population of BHs we are sensitive to, in this section we explore the AGN detection limit for the low-mass sample, given the depth of the SDSS observations and the difference imaging technique. For each light curve, we compute the median nucleus g -band magnitude and the standard deviation of the individual measurements about the median magnitude (σ_{LC}). Thus for a given magnitude bin, we can compute the median light curve standard deviation of objects in that bin. For example, the median σ_{LC} for nuclei with an apparent g -band magnitude of 18 is 0.01 mag. For nuclei with apparent g -band magnitude of 20, the median σ_{LC} is 0.035 mag. The nuclei selected as having AGN-like variability all have light curve standard deviations $\gtrsim 1\sigma$ above the median σ_{LC} for their magnitude bin (see Figure 5).

We next compute the typical galaxy magnitude within the $2''.5$ nuclear aperture as a function of redshift. For a given redshift bin, we use the median Sérsic profile index (as given by the NSA) to determine the typical fraction of galaxy light contained within $2''.5$. We then use this value to compute the typical g -band magnitude within $2''.5$. As mentioned above, each magnitude has a light curve standard deviation value above which the objects classified as AGNs are found. For each redshift, we convert the variations in the apparent magnitude to variations in the luminosity. Then, assuming that the observed variations are on order 10% or 50% of the total AGN luminosity, we compute the total g -band luminosity an AGN would need to have to be detectable in a typical galaxy of a given stellar mass as a function of redshift (top panels of Figure 11).

We stress that this analysis comprises a rough estimate of our detection limits—at any stellar mass, there exist galaxies with a wide range of Sérsic indices and luminosities and thus a range of AGN luminosities/BH masses that could be detected. Nevertheless, based on this calculation, we can roughly expect

Table 1
Candidate Variability-selected AGNs in Low-mass Galaxies

NSA ID ^a	R.A.	Decl.	Redshift	$\log_{10}\left(\frac{M_*}{M_\odot}\right)$	m_g	Rms	σ_{var}	σ_{QSO}	σ_{noQSO}	BPT Class	$\log_{10}\left(\frac{M_{\text{BH}}}{M_\odot}\right)$
31861	358.35750	-0.506680	0.0234	6.73E+08	18.574	0.0300	3.753	2.297	0.025	SF	...
32083	0.47615	0.125693	0.1395	7.69E+09	19.072	0.1155	17.503	2.951	1.447	AGN	7.2
32653	2.36003	0.325606	0.1138	2.94E+09	19.963	0.0623	3.823	2.705	0.216	AGN	6.8
33205	4.27033	-0.493348	0.0672	9.35E+09	17.653	0.0150	2.246	2.346	0.001	Comp	6.6
33611	6.96605	0.794382	0.0821	6.26E+09	17.994	0.0231	4.25	2.674	0.004	SF	...
33835	8.39416	0.048925	0.1067	8.03E+09	19.179	0.0376	3.87	2.753	0.004	SF	...
33851	8.15918	-1.009817	0.0917	9.15E+09	17.826	0.0507	14.746	3.762	0.196	Comp	6.8
34071	11.38946	-0.969121	0.1376	7.40E+09	18.920	0.1477	28.678	4.81	0.928	AGN	6.6
34281	11.51401	0.636591	0.1246	3.81E+09	18.346	0.0232	2.853	2.055	0.012	SF	...
34728	14.01926	0.592550	0.0560	7.76E+09	17.884	0.0193	2.721	2.122	0.004	Comp	...
35245	16.14294	-1.042719	0.0746	1.65E+09	18.923	0.0495	8.225	3.044	0.118	SF	...
35813	18.74797	0.245735	0.0426	6.73E+08	18.953	0.0320	3.457	3.167	0.0	SF	...
35920	19.87115	-0.144376	0.0901	7.91E+09	17.875	0.0587	18.336	2.54	1.491	Comp	6.5
36541	21.64659	0.144874	0.1194	6.14E+09	19.349	0.0940	15.997	4.408	0.093	SF	...
38331	33.44361	-0.831365	0.0933	4.44E+09	18.315	0.0318	6.151	4.267	0.0	SF	...
38720	36.53416	-0.888560	0.1065	5.68E+09	18.200	0.0304	6.965	2.856	0.05	AGN	6.7
39920	44.96551	-0.256340	0.1014	9.40E+09	19.219	0.2410	46.447	5.929	1.741	...	7.8
40018	45.70326	0.358798	0.1070	7.84E+09	19.340	0.1680	31.455	4.169	2.938	AGN	7.5
40170	48.25895	-0.686379	0.1312	6.24E+09	19.535	0.0755	9.191	3.884	0.079	AGN	7.0
40182	47.61596	-0.830791	0.0802	5.46E+09	16.168	0.180	109.36	4.362	4.66	Comp	7.6
40677	49.42965	0.326904	0.0687	5.02E+09	17.961	0.024	6.432	2.851	0.0133	Comp	6.1
112799	346.84687	0.285572	0.1128	9.83E+09	18.686	0.0588	12.278	3.206	0.587	AGN	7.1
113167	354.59937	1.226183	0.0637	2.28E+09	18.375	0.0218	2.897	3.604	0.0	SF	...
114482	17.68218	0.423656	0.0823	8.32E+09	18.958	0.0366	3.109	2.402	0.004
114617	20.15146	0.601762	0.1249	7.80E+08	19.861	0.0548	2.911	2.615	0.005	SF	...
115553	43.73940	0.432075	0.1077	1.58E+09	19.251	0.0316	2.314	3.278	0.0	SF	...
141699	47.72545	1.030173	0.1233	6.41E+09	19.934	0.0473	2.032	2.102	0.008	Comp	...
204319	330.36643	-0.800648	0.1102	9.18E+09	19.083	0.1083	15.312	2.924	0.8	AGN	7.9
214788	27.36857	1.028639	0.0581	1.59E+09	19.182	0.0549	7.657	2.835	0.088	SF	...
215903	8.240055	-0.454011	0.1070	1.65E+09	19.852	0.0470	2.204	2.021	0.02	SF	...
217124	331.50298	0.913803	0.0411	2.84E+08	20.062	0.0931	5.603	3.06	0.028	SF	...
305046	19.50434	-0.496008	0.0911	6.27E+09	19.293	0.0423	3.738	2.765	0.01	AGN	6.6
305680	29.26929	-1.179740	0.0823	1.52E+09	19.196	0.0389	4.13	2.284	0.028	SF	...
310445	46.12571	0.344850	0.1260	4.23E+09	20.652	0.0688	2.502	3.712	0.0	SF	...
583482	336.14706	-0.184434	0.0580	9.61E+09	17.168	0.1295	61.768	3.413	3.495	AGN	7.6

Notes. Galaxies with light curves that meet our selection criteria for having an AGN, i.e., $\sigma_{\text{var}} > 2$ and a QSO significance $\sigma_{\text{qso}} > 2$. Galaxies are ordered from lowest to highest stellar mass.

^a NSA ID from nsa_v1_0_1.fits catalog.

to detect a $\sim 10^5 M_\odot$ BH in a low-mass galaxy accreting at its Eddington luminosity and varying at the 10% level out to $z \approx 0.05$. For luminosity variations on the 50% level, the same should be detectable to $z \approx 0.1$.

5.2. Expected Number of Detections

We next explore how many variable AGNs we could expect to detect in our $M_* < 10^{10} M_\odot$ sample, given local scaling relations between BH mass and the host galaxy. Using the relations between BH mass and stellar mass from Reines & Volonteri (2015), we assign each galaxy a BH mass given its stellar mass in the NSA (and given the intrinsic scatter in the $M_{\text{BH}}-M_*$ relation). Reines & Volonteri (2015) find different $M_{\text{BH}}-M_*$ relations for inactive elliptical/S0 galaxies and local active broad-line AGNs; we test both relations. For each of the $M_{\text{BH}}-M_*$ relations, we then compute bolometric luminosities by applying the Eddington ratio distribution given by Bernhard et al. (2018) for low-mass galaxies ($10^8-10^{10} M_\odot$). We can then determine how many galaxies would be detected, assuming the g-band luminosity is 5% of the total bolometric luminosity, and luminosity variations at the 10% or 50% level.

Table 2
Active Fraction across Apparent Magnitude Bins

Mag. bin	$F_{\text{AGN}} (M_* < 10^{10} M_\odot)$	$F_{\text{AGN}} (M_* > 10^{10} M_\odot)$
16	0/22	2/123
17	1/180	15/738
18	10/1535	41/2895
19	17/6535	39/5878
20	6/7292	2/1305
21	1/1163	0/55

Note. This table gives the number of high- and low-mass galaxies in a given magnitude bin (denominator) and the number of objects with AGN-like variability in that bin.

In Figure 11, we show the minimum detectable AGN luminosity (as discussed in the previous section), along with examples of simulated BH samples given both $M_{\text{BH}}-M_*$ relations and luminosity variation level. We also show the histograms of the number of detected AGNs for 100 simulated samples using each combination of $M_{\text{BH}}-M_*$ relation and luminosity variation level. For BH masses populated according to the $M_{\text{BH}}-M_*$ relation for

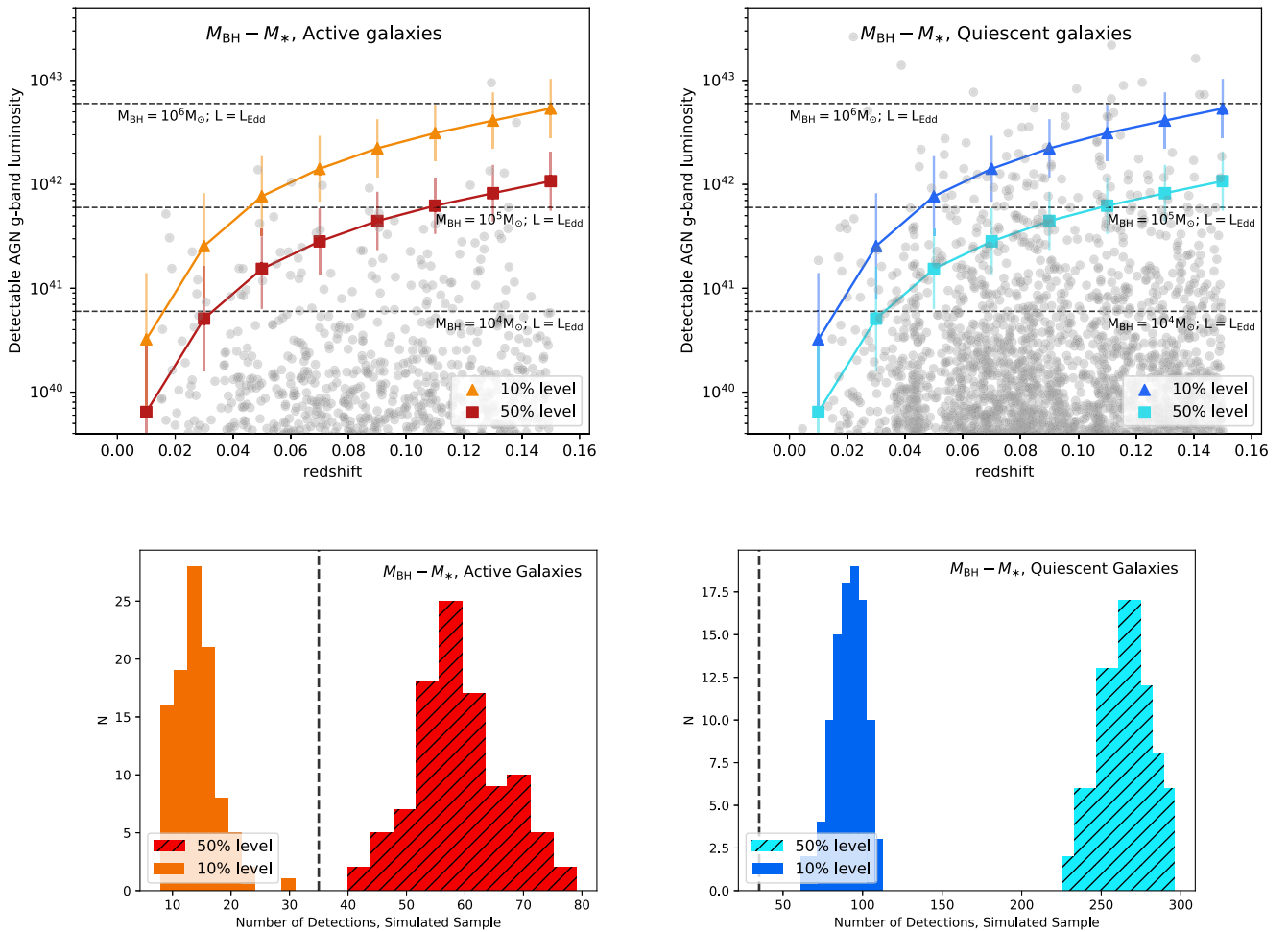


Figure 11. Top row: detectable AGN g -band luminosity vs. redshift. Each plot shows the minimum g -band luminosity an AGN would need to have to be detectable as a function of redshift, if the luminosity is varying at the 10% level (triangles) and 50% level (squares). Black dashed lines mark the g -band luminosities of BHs ranging from 10^4 to $10^6 M_{\odot}$, if they are accreting at their Eddington luminosity (and given that $\sim 5\%$ of the luminosity is emitted in the g -band, based on AGN spectral energy densities from Richards et al. 2006). In each plot we also show a simulated sample of BHs, given the the $M_{\text{BH}} - M_*$ relations in Reines & Volonteri (2015) for active galaxies (left) and quiescent galaxies (right), and an Eddington ratio distribution (Bernhard et al. 2018). See the text for more details on the computation of the minimum detectable luminosity. Bottom row: we create 100 simulated BH samples for each combination of $M_{\text{BH}} - M_*$ relation and luminosity variation level. These histograms show the number of detectable objects per simulated sample. On the left, we show the number of detections in simulated BH samples based on the $M_{\text{BH}} - M_*$ relation for local active galaxies, for luminosity variations at the 10% (orange) or 50% (red hatched) level. On the right, we show the number of detections in simulated BH samples based on the $M_{\text{BH}} - M_*$ relation for quiescent elliptical/S0 galaxies, for luminosity variations at the 10% (dark blue) or 50% (turquoise hatched) level. The dashed black line marks our actual number of detected variable AGNs for the low-mass sample.

elliptical/S0 galaxies, we expect to detect 92 ± 10.4 variable AGNs for variations at the 10% level, and 264 ± 15.6 for 50% variations. For BH masses populated according to the $M_{\text{BH}} - M_*$ relation for local active galaxies, we expect to detect 13.5 ± 3.6 for 10% variations, and 58 ± 7.6 for 50% variations. Our detected number of low-mass galaxies with AGN-like variability—35—is more closely in line with the number expected based on the $M_{\text{BH}} - M_*$ relation for active galaxies.

5.3. Comparison to Other Low-mass AGN Selection Techniques

One of the most effective techniques for identifying AGNs in low-mass galaxies is optical spectroscopy. Reines et al. (2013) searched for AGNs in dwarf galaxies (defined as galaxies with $M_* < 3 \times 10^9 M_{\odot}$) in the NSA using optical narrow emission-line ratio selection criteria. Of $\sim 25,000$ dwarf galaxies, 136 had narrow emission-line signatures indicative of AGN activity, for a detection fraction of 0.5%. Ten of them also had broad $\text{H}\alpha$ emission, with BH masses ranging from 8×10^4

to $1 \times 10^6 M_{\odot}$. Our sample contains 8941 galaxies with $M_* < 3 \times 10^9 M_{\odot}$, 12 of which have AGN-like variability. This gives a variability detection fraction of 0.1%. Of the 12 dwarf galaxies with AGN-like variability, one (NSA 32653) has narrow emission-line ratios in the AGN region of the BPT diagram and shows broad $\text{H}\alpha$ emission ($M_{\text{BH}} = 6 \times 10^6 M_{\odot}$). It was not selected in Reines et al. (2013), as that work used the NSA v0, which only extends out to $z = 0.055$.

Moran et al. (2014) also used optical spectroscopy to search for AGNs in low-mass galaxies. Specifically, they searched for AGN signatures in galaxies with $M_* < 10^{10} M_{\odot}$ within 80 Mpc. Overall, they detected AGNs in 28/9526 galaxies, for a detection fraction of 0.29% (similar to our detection fraction of 0.22%). Of their 28 galaxies, seven have stellar masses in the regime considered by Reines et al. (2013), five of which are also classified as AGNs in that work. When considering just galaxies with stellar masses between 4×10^9 and $10^{10} M_{\odot}$, their detection fraction is 2.7%. The Moran et al. (2014) AGN host galaxies have a median $g - r$ color of 0.62, slightly redder than our sample.

There are six dwarf galaxies with narrow emission-line evidence for AGN activity from Reines et al. (2013) which fall inside the area covered by the Stripe 82 survey (none of the Moran et al. 2014 objects fall within Stripe 82). None is classified as having nuclear variability according to our selection criteria. One of the six galaxies (RGG 1 in Reines et al. 2013) has broad H α emission, from which we can obtain a BH mass estimate. RGG 1 is at a redshift of 0.046 and has a stellar mass of $2.6 \times 10^9 M_\odot$. The BH mass reported in Reines et al. (2013) is $5.0 \times 10^5 M_\odot$ (note that systematic uncertainties on BH masses derived from broad H α are on the order of ~ 0.3 dex). Using *Chandra* X-ray observations, Baldassare et al. (2017b) find that this BH is accreting at $0.001 L_{\text{Edd}}$. Using the same assumptions as the previous section, this BH would have a *g*-band luminosity of $3.0 \times 10^{39} \text{ erg s}^{-1}$. As shown in Figure 11, at a redshift of 0.05, we are sensitive to AGNs with *g*-band luminosities greater than $\sim 10^{41} \text{ erg s}^{-1}$. Therefore, we would not expect to detect any variability from this AGN (see Figure 11).

6. Discussion and Conclusions

We analyze the light curves of $\sim 28,000$ nearby ($z < 0.15$) galaxies in the SDSS Stripe 82 field for AGN-like nuclear variability. We concentrate our analysis on galaxies in the NSA, which have spectroscopic redshifts and stellar mass estimates. We construct light curves using difference imaging, which allows us to detect small variations superposed on top of the stellar light from the galaxy. We then determine whether variability is AGN-like by assessing how well individual light curves are described by a damped random walk.

We find 135 galaxies with AGN-like variability. The variability-selected sample spans roughly four orders of magnitude in stellar mass. Above $M_* = 10^{10} M_\odot$ (100 galaxies), almost all of the variability-selected AGNs also have narrow emission-line ratios in the AGN or composite regions of the BPT diagram. Below $M_* = 10^{10} M_\odot$, half of the galaxies have narrow emission-line ratios dominated by star formation, indicating they may be AGNs missed by other selection techniques due to star formation dilution or metallicity effects, which are expected to be more important at lower stellar masses. We stress that the low-mass galaxies with AGN-like variability falling in the star-forming region of the BPT diagram should be regarded as candidates; we are in the process of obtaining higher spatial resolution follow-up spectroscopy which better isolates emission from the nucleus. High spatial resolution X-ray and/or radio observations will also be valuable in the effort to confirm the presence of AGNs in these systems.

Using this sample, we study the fraction of variable AGNs as a function of stellar mass, and find that even when accounting for magnitude bias, there is a decline in the fraction of variable AGNs with decreasing stellar mass. The low active fraction for low-mass galaxies could be attributed to a lower BH occupation fraction for galaxies with $M_* < 10^{10} M_\odot$, a change in the $M_{\text{BH}}-M_*$ relation for low-mass galaxies, or a change in the variability properties of BHs in low-mass galaxies. We discuss these possible explanations below.

A drop in the *occupation fraction* (i.e., the fraction of galaxies with BHs) at low galaxy stellar mass would lead naturally to a drop in the fraction hosting active BHs. While it is well established that the occupation fraction for massive galaxies is 100% (or extremely close; Magorrian et al. 1998), it is unclear whether that holds for low-mass galaxies. Nguyen et al. (2017, 2018) obtained dynamical detections of central BHs in five nearby low-mass early-type galaxies ($M_{\text{BH}} = 10^9-10^{10} M_\odot$),

and find that four of the five have detected central BHs, for an 80% occupation fraction. However, there are several nearby galaxies for which there are stringent limits on the mass of a central BH based on dynamical modeling; for example, Gebhardt et al. (2001) find that the upper limit on a central BH in M33 is just $1500 M_\odot$. There are ongoing efforts to constrain the BH occupation fraction at low masses using X-ray observations; current estimates place a firm lower limit of 20% on the low-mass occupation fraction (Miller et al. 2015).

Another possibility is that $M_{\text{BH}}-M_*$ is lower for low-mass galaxies than for more massive galaxies. Massive galaxies show a fairly constant (with some scatter) ratio between the mass of the central BH and the mass of the galaxy ($\sim 1/1000$ or 0.001). Recent works have shown that BHs in low-mass galaxies may be under-massive with respect to the scaling relations between BH mass and bulge/galaxy stellar mass defined for more massive galaxies (Greene et al. 2008; Reines & Volonteri 2015; Baldassare et al. 2017a). One explanation for this is bimodal accretion at high redshift, whereby accretion is inefficient below a certain mass threshold (Pacucci et al. 2018). As mentioned above, we estimate BH masses for the 16 low-mass galaxies with broad H α emission. They range from $\log(M_{\text{BH}}/M_\odot) = 6.0$ to 7.9 (with uncertainties of ~ 0.3 dex). The median BH mass is $\log(M_{\text{BH}}/M_\odot) = 6.8$. These masses correspond to $M_{\text{BH}}-M_*$ values of 0.0002–0.007 (median $M_{\text{BH}}-M_* = 0.0013$). Thus, we may only be able to detect variable AGNs (with this data set) in the low-mass galaxies that have unusually massive BHs (as compared to other galaxies of similar stellar mass).

Finally, it is possible that AGNs in low-mass galaxies are intrinsically less variable, or are less variable at optical wavelengths. Monitoring campaigns of known low-mass galaxies with AGNs will be important for studying whether such galaxies vary on similar timescales and/or with similar amplitudes as more massive AGNs.

The objects with AGN-like variability falling in the star-forming region of the BPT diagram will require multi-wavelength follow-up to search for additional evidence for AGNs in these systems. Our analysis will also be extended to additional existing repeat imaging surveys to search for more low-mass systems with AGN-like variability. The Large Synoptic Survey Telescope will be ideal for continuing searches for low-level variability on days-to-months timescales and should be sensitive to less massive BHs and/or BHs accreting at lower Eddington fractions.

Support for V.F.B. was provided by the National Aeronautics and Space Administration through Einstein Postdoctoral Fellowship Award Number PF7-180161 issued by the *Chandra X-ray Observatory* Center, which is operated by the Smithsonian Astrophysical Observatory for and on behalf of the National Aeronautics Space Administration under contract NAS8-03060. The authors thank Michael Tremmel and Michael Warrenner for useful comments which have improved this paper.

Software: Astropy (The Astropy Collaboration et al. 2018), DIAPL2 (Wozniak 2000), QSO_fit (Butler & Bloom 2011).

Appendix Light Curves of Low-mass Galaxies with AGN-like Variability

Figure 12 shows light curves and DECaLS imaging for all objects with NSA stellar masses $M_* < 10^{10} M_\odot$. The objects are in order of NSA ID.

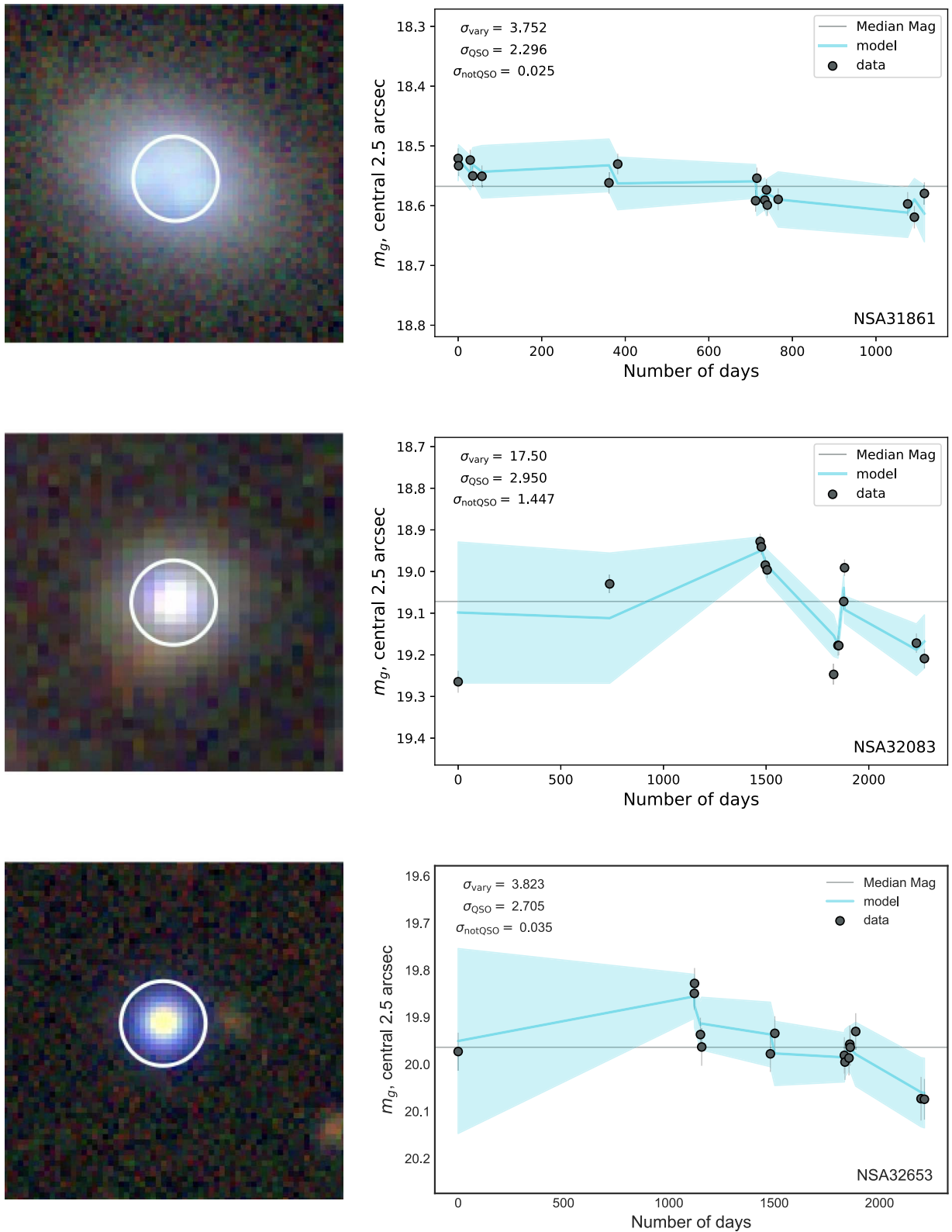


Figure 12. DECaLS imaging and SDSS g -band light curves of low-mass galaxies ($M_* < 10^{10} M_\odot$) which meet our AGN variability selection criteria. The gray points are the observed nuclear g -band magnitudes with corresponding errors. The blue solid line shows the best fit damped random walk model from `qso_fit`, and the light blue shaded region shows the model uncertainties. This example shows galaxies NSA 31861, NSA 32083, and NSA 32653.

(The complete figure set (35 images) is available.)

ORCID iDs

Vivienne F. Baldassare  <https://orcid.org/0000-0003-4703-7276>
 Marla Geha  <https://orcid.org/0000-0002-7007-9725>

References

- Aihara, H., Allende Prieto, C., An, D., et al. 2011, *ApJS*, 193, 29
 Alard, C. 2000, *A&AS*, 144, 363
 Alard, C., & Lupton, R. H. 1998, *ApJ*, 503, 325
 Baldassare, V. F., Reines, A. E., Gallo, E., et al. 2016, *ApJ*, 829, 57
 Baldassare, V. F., Reines, A. E., Gallo, E., & Greene, J. E. 2015, *ApJL*, 809, L14
 Baldassare, V. F., Reines, A. E., Gallo, E., & Greene, J. E. 2017a, *ApJ*, 850, 196
 Baldassare, V. F., Reines, A. E., Gallo, E., & Greene, J. E. 2017b, *ApJ*, 836, 20
 Baldwin, J. A., Phillips, M. M., & Terlevich, R. 1981, *PASP*, 93, 5
 Barth, A. J., Greene, J. E., & Ho, L. C. 2008, *AJ*, 136, 1179
 Barth, A. J., Voevodkin, A., Carson, D. J., & Woźniak, P. 2014, *AJ*, 147, 12
 Bellm, E. 2014, in *The Third Hot-wiring the Transient Universe Workshop*, ed. P. R. Woźniak et al., 27
 Bentz, M. C., Denney, K. D., Grier, C. J., et al. 2013, *ApJ*, 767, 149
 Bentz, M. C., Walsh, J. L., Barth, A. J., et al. 2009, *ApJ*, 705, 199
 Bentz, M. C., Walsh, J. L., Barth, A. J., et al. 2010, *ApJ*, 716, 993
 Bernhard, E., Mullaney, J. R., Aird, J., et al. 2018, *MNRAS*, 476, 436
 Blanton, M. R., Kazin, E., Muna, D., Weaver, B. A., & Price-Whelan, A. 2011, *AJ*, 142, 31
 Blanton, M. R., & Roweis, S. 2007, *AJ*, 133, 734
 Bradford, J. D., Geha, M. C., Greene, J. E., Reines, A. E., & Dickey, C. M. 2018, *ApJ*, 861, 50
 Butler, N. R., & Bloom, J. S. 2011, *AJ*, 141, 93
 Cartier, R., Lira, P., Coppi, P., et al. 2015, *ApJ*, 810, 164
 Chambers, K. C., Magnier, E. A., Metcalfe, N., et al. 2016, arXiv:1612.05560
 Choi, Y., Gibson, R. R., Becker, A. C., et al. 2014, *ApJ*, 782, 37
 Flewelling, H. A., Magnier, E. A., Chambers, K. C., et al. 2016, arXiv:1612.05243
 Gaia Collaboration, Prusti, T., de Bruijne, J. H. J., et al. 2016, *A&A*, 595, A1
 Gebhardt, K., Lauer, T. R., Kormendy, J., et al. 2001, *AJ*, 122, 2469
 Geha, M., Alcock, C., Allsman, R. A., et al. 2003, *AJ*, 125, 1
 Greene, J. E. 2012, *NatCo*, 3, 1304
 Greene, J. E., & Ho, L. C. 2004, *ApJ*, 610, 722
 Greene, J. E., & Ho, L. C. 2005, *ApJ*, 630, 122
 Greene, J. E., & Ho, L. C. 2007, *ApJ*, 670, 92
 Greene, J. E., Ho, L. C., & Barth, A. J. 2008, *ApJ*, 688, 159
 Groves, B. A., Heckman, T. M., & Kauffmann, G. 2006, *MNRAS*, 371, 1559
 Heinis, S., Gezari, S., Kumar, S., et al. 2016, *ApJ*, 826, 62
 Ho, L. C., Filippenko, A. V., Sargent, W. L. W., & Peng, C. Y. 1997, *ApJS*, 112, 391
 Izotov, Y. I., & Thuan, T. X. 2009, *ApJ*, 690, 1797
 Kelly, B. C., Bechtold, J., & Siemiginowska, A. 2009, *ApJ*, 698, 895
 Kewley, L. J., Dopita, M. A., Leitherer, C., et al. 2013, *ApJ*, 774, 100
 Kewley, L. J., Dopita, M. A., Sutherland, R. S., Heisler, C. A., & Trevena, J. 2001, *ApJ*, 556, 121
 Kewley, L. J., Groves, B., Kauffmann, G., & Heckman, T. 2006, *MNRAS*, 372, 961
 Kormendy, J., & Ho, L. C. 2013, *ARA&A*, 51, 511
 Kumar, S., Gezari, S., Heinis, S., et al. 2015, *ApJ*, 802, 27
 LaMassa, S. M. 2017, *AN*, 338, 323
 Lehmer, B. D., Alexander, D. M., Bauer, F. E., et al. 2010, *ApJ*, 724, 559
 Lemons, S. M., Reines, A. E., Plotkin, R. M., Gallo, E., & Greene, J. E. 2015, *ApJ*, 805, 12
 MacLeod, C. L., Brooks, K., Ivezić, Ž., et al. 2011, *ApJ*, 728, 26
 MacLeod, C. L., Ivezić, Ž., Kochanek, C. S., et al. 2010, *ApJ*, 721, 1014
 Magorrian, J., Tremaine, S., Richstone, D., et al. 1998, *AJ*, 115, 2285
 Matsuoka, Y., Strauss, M. A., Price, T. N., III, & DiDonato, M. S. 2014, *ApJ*, 780, 162
 Mezcua, M., Civano, F., Fabbiano, G., Miyaji, T., & Marchesi, S. 2016, *ApJ*, 817, 20
 Mezcua, M., Civano, F., Marchesi, S., et al. 2018, *MNRAS*, 478, 2576
 Miller, B. P., Gallo, E., Greene, J. E., et al. 2015, *ApJ*, 799, 98
 Mineo, S., Gilfanov, M., & Sunyaev, R. 2012, *MNRAS*, 419, 2095
 Moran, E. C., Shahinyan, K., Sugarman, H. R., Vélez, D. O., & Eracleous, M. 2014, *AJ*, 148, 136
 Morokuma, T., Tominaga, N., Tanaka, M., et al. 2016, *PASJ*, 68, 40
 Natarajan, P. 2014, *GR&Gr*, 46, 1702
 Nguyen, D. D., Seth, A. C., den Brok, M., et al. 2017, *ApJ*, 836, 237
 Nguyen, D. D., Seth, A. C., Neumayer, N., et al. 2018, *ApJ*, 858, 118
 Pacucci, F., Loeb, A., Mezcua, M., & Martín-Navarro, I. 2018, *ApJL*, 864, L6
 Palanque-Delabrouille, N., Yèche, C., Myers, A. D., et al. 2011, *A&A*, 530, A122
 Pardo, K., Goulding, A. D., Greene, J. E., et al. 2016, *ApJ*, 831, 203
 Rau, A., Kulkarni, S. R., Law, N. M., et al. 2009, *PASP*, 121, 1334
 Rees, M. J. 1984, *ARA&A*, 22, 471
 Reines, A. E., Greene, J. E., & Geha, M. 2013, *ApJ*, 775, 116
 Reines, A. E., Plotkin, R. M., Russell, T. D., et al. 2014, *ApJL*, 787, L30
 Reines, A. E., Sivakoff, G. R., Johnson, K. E., & Brogan, C. L. 2011, *Natur*, 470, 66
 Reines, A. E., & Volonteri, M. 2015, *ApJ*, 813, 82
 Richards, G. T., Lacy, M., Storrie-Lombardi, L. J., et al. 2006, *ApJS*, 166, 470
 Schmidt, K. B., Marshall, P. J., Rix, H.-W., et al. 2010, *ApJ*, 714, 1194
 Secrest, N. J., Satyapal, S., Gliozzi, M., et al. 2015, *ApJ*, 798, 38
 Sesar, B., Ivezić, Ž., Lupton, R. H., et al. 2007, *AJ*, 134, 2236
 The Astropy Collaboration, Price-Whelan, A. M., Sipőcz, B. M., et al. 2018, *AJ*, 156, 123
 Trump, J. R., Sun, M., Zeimann, G. R., et al. 2015, *ApJ*, 811, 26
 Woźniak, P. R. 2000, *AcA*, 50, 421
 Yan, R. 2011, *AJ*, 142, 153